IEEE Access
Multidisciplinary | Rapid Review | Open Access Journal

Received October 27, 2020, accepted November 8, 2020, date of publication November 16, 2020,
date of current version November 24, 2020.

Digital Object Identifier 10.1109/ACCESS.2020.3037811

Forward Analysis of GPR for Underground Pipes Using CUDA-Implemented Conformal Symplectic Euler Algorithm

JIANWEI LEI, BINGHAN XUE, HONGYUAN FANG, YINPING LI, AND MAN YANG
School of Water Conservancy Engineering, Zhengzhou University, Zhengzhou 450001, China

Corresponding authors: Binghan Xue (xuebinghan@zzu.edu.cn) and Hongyuan Fang (18337192244@163.com)

This work was supported in part by the National Key Research and Development Program of China under Grant 2017YFC1501204, in part by the National Natural Science Foundation of China under Grant 51678536 and Grant 11771407, in part by the Program for Science and Technology Innovation Talents in Universities of Henan Province under Grant 19HASTIT043, in part by the Outstanding Young Talent Research Fund of Zhengzhou University under Grant 1621323001, in part by the Program for Innovative Research Team (in Science and Technology) in University of Henan Province under Grant 18IRTSTHN007, and in part by the Transportation Science and Technology Project of Henan Province under Grant 2018J7.

ABSTRACT Ground-penetrating radar (GPR) is widely used in the detection and positioning of underground facilities. Through the inversion analysis of echo signals of GPR, information such as pipe material, burial depth and location of pipelines can be obtained. Unfortunately, underground pipelines are cylindrical, the ladder approximation method used in traditional forward models produces certain errors. In this study, an accurate and efficient numerical model of GPR forward model in underground pipelines is established using symplectic Euler algorithm, graphics processing unit (GPU) acceleration technology and surface conformal technology. With a Ricker wavelet pulse as the GPR source, the convolution perfectly matched layer (CPML) is incorporated in the symplectic Euler algorithm and shown to be effective to truncate the symplectic Euler computational domain. Through the simulation study of different underground pipeline models, GPR image characteristics of the metal pipeline, plastic pipeline and concrete pipeline filled with air and water are obtained. According to the numerical simulation results, parallel conformal symplectic Euler algorithm effectively reduces the false diffracted waves caused by ladder approximation and improves the computational efficiency of the model in metallic and non-metallic media.

INDEX TERMS GPR, underground pipeline, numerical simulation, symplectic Euler algorithm, surface conformal technology, parallel computing.

I. INTRODUCTION

With the developing and utilizing of underground space, the scale of the underground pipeline network has been continuously expanded, and various pipeline networks, such as those for water, drainage, gas, heat, electricity, and communications, are as dense as nets [1]. However, because the pipelines are constructed and managed by multiple entities and construction management is inadequate, the distribution information of underground pipeline networks is scant. Accidents from excavating existing pipeline networks often occur in the construction of municipal infrastructure and building foundation pits, which leads to large economic losses and has seriously affected the life of residents. The quick and accurate determination of the location and material of underground pipelines has become an urgent problem to be solved in urban construction projects [2].

Pipeline detectors are currently the most commonly used equipment for urban underground pipeline detection, but such equipment can only detect metal pipelines. GPR tomography is an effective method to detect underground strata and buried objects. Featuring high resolution, real-time display and flexible use, GPR tomography can be applied to detect both metal and non-metallic pipelines. As an effective detection method, GPR technology has broad application prospects in the nondestructive detection of underground pipeline structures [3]–[6]. Through inversion analysis of the signals measured by GPR, information such as the position, material and burial depth of pipelines can be obtained [7]–[10]. An efficient and accurate numerical

The associate editor coordinating the review of this manuscript and approving it for publication was Muhammad Zubair.

model of electromagnetic wave propagation in underground pipeline GPR is the premise of inversion of measured signals [4], [11]–[16].

In order to accurately interpret the measured GPR images of underground pipes, it is necessary to study the GPR data numerical simulation of underground pipes, and evaluate what useful information can be reasonably extracted from the field data under various conditions [17]–[21]. In the previous study, we established an accurate and efficient forward model based on the symplectic Euler algorithm, surface conformal technology and GPU acceleration technology to simulate the circular cavity disease in pavement structure [22], [23]. However, the CPML boundary was not used in the previous simulation, and the absorption at the boundary was poor. In this paper, the CPML boundary suitable for symplectic algorithm was derived and applied to the underground pipeline simulation. In the previous simulation study [24], surface conformal technology was only applied to the simulation of non-metallic media. In this paper, the surface conformal technique in metal and non-metal media was applied to metal pipe and concrete pipe model simulation.

An accurate and efficient GPR forward model of underground pipeline structures is established based on the symplectic Euler algorithm, GPU acceleration technology, and surface conformal technology. Firstly, the calculation results of serial non-conformal and parallel conformal symplectic Euler algorithm are compared by a circular void model to verify the efficiency and accuracy of the proposed algorithm. Then, through the simulation study of different underground pipeline models, the significant characteristics of GPR data of the metal pipeline, plastic pipeline and concrete pipeline filled with air and water are reproduced. This paper is organized as follows. Section II is devoted to a description of the symplectic Euler algorithm and CPML boundary conditions. Section III presents the surface conformal technology of metal and nonmetal media and the GPU acceleration technology, while in Section IV, the results of the different underground pipeline numerical simulations results are discussed and analyzed. Conclusions are drawn in Section V.

II. METHODOLOGY

A. CONTROL EQUATIONS

In an isotropically lossy medium, the Maxwell equations are expressed as

$$\begin{aligned}\frac{\partial \boldsymbol{E}}{\partial t} &= \frac{1}{\varepsilon}\nabla \times \boldsymbol{H} - \frac{\sigma}{\varepsilon}\boldsymbol{E} \\ \frac{\partial \boldsymbol{H}}{\partial t} &= -\frac{1}{\mu}\nabla \times \boldsymbol{E}\end{aligned} \tag{1}$$

where $\boldsymbol{H}$ and $\boldsymbol{E}$ represent the magnetic field and electric field vector, respectively, σ, ε, and μ are the electrical conductivity, dielectric constant, and magnetic conductivity.

Introducing the vector magnetic potential $\boldsymbol{H} = \nabla \times \boldsymbol{A}$ and letting $\boldsymbol{E} = -\boldsymbol{U}$ [25], [26], the Maxwell equations in the lossy system can be written as

$$\begin{aligned}\frac{\partial \boldsymbol{A}}{\partial t} &= \frac{\partial \mathrm{H}}{\partial \boldsymbol{U}} = \frac{1}{\mu}\boldsymbol{U} \\ \frac{\partial \boldsymbol{U}}{\partial t} &= \frac{\partial \mathrm{H}}{\partial \boldsymbol{A}} = \frac{1}{\varepsilon}\nabla \times \nabla \times \boldsymbol{A} - \frac{\sigma}{\varepsilon}\boldsymbol{U}\end{aligned} \tag{2}$$

For the two-dimensional Transverse Magnetic (TM) wave, (2) can be reduced to

$$\begin{aligned}\frac{\partial \boldsymbol{A}_z}{\partial t} &= \frac{1}{\mu}\boldsymbol{U}_z \\ \frac{\partial \boldsymbol{U}_z}{\partial t} &= \frac{1}{\varepsilon}\nabla^2 \boldsymbol{A}_z - \frac{\sigma}{\varepsilon}\boldsymbol{U}_z\end{aligned} \tag{3}$$

where $\boldsymbol{U}_z$ and $\boldsymbol{A}_z$ are the components of the field components $\boldsymbol{U}$ and $\boldsymbol{A}$ along the z direction, and ∇^2 is the Laplacian operators. The second order central difference is used to discretize the Laplacian operator.

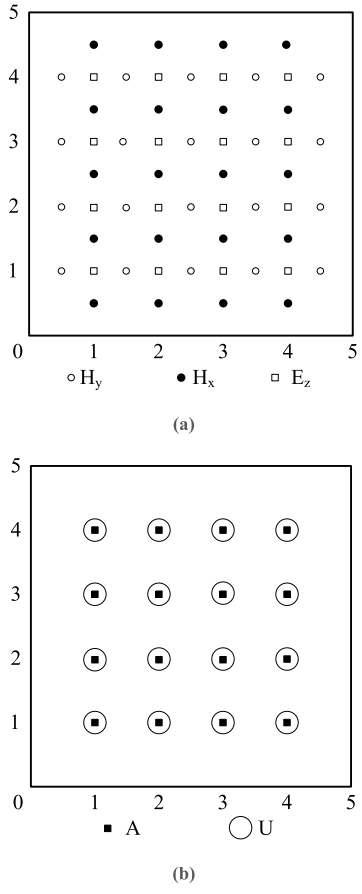

FIGURE 1. Spatial distribution of two-dimensional TM wave field components. (a) Spatial distribution of wave field components gained by FDTD method. (b) Spatial distribution of wave field components obtained by symplectic Euler algorithm.

The FDTD method uses the Yee grid to discretize the partial differential operator in the Maxwell degree equations. The electric and magnetic fields are separated in time and space by half time and spatial steps, i.e., the electric field is located in the center of the unit, which is surrounded by the magnetic field (Fig. 1(a)). The symplectic Euler algorithm

is discretely defined by the electric field and magnetic field in the same spatial grid node and time step (Fig. 1(b)). This discrete grid method is more suitable for processing complex problems regarding boundaries [27]. Using symplectic Euler algorithm to discrete (3), the iterative equation is obtained as

$$\begin{aligned} A_{i,j}^{n+1} &= A_{i,j}^{n} + \frac{dt}{\mu} U_{i,j}^{n} \\ U_{i,j}^{n+1} &= \frac{\varepsilon - dt\sigma}{\varepsilon} U_{i,j}^{n} + \frac{dt}{\varepsilon} \nabla^2 A_{i,j}^{n+1} \end{aligned} \tag{4}$$

Here, $A_{i,j}^{n}$ and $U_{i,j}^{n}$ represent the discrete values of the field components $\boldsymbol{A}_z$ and $\boldsymbol{U}_z$ at spatial grid node at time $n$dt.

B. ABSORBING BOUNDARY CONDITION

GPR electromagnetic wave propagation in underground structures is an open-domain problem, so reasonable absorption boundary conditions must be set at the cutoff boundary of the calculation area. The convolutional perfectly matched layer (CPML) boundary [28], [29] with good absorption effect is used in this study. In the lossy medium 2D symplectic Euler algorithm, the CPML equation can be expressed as

$$\begin{aligned} U_z^{n+1}(i,j,k) &= \frac{\Delta t}{\varepsilon s_z}\left(\frac{\partial^2 A_z^{n+1}}{\partial x^2} + \frac{\partial^2 A_z^{n+1}}{\partial y^2}\right) \\ &\quad + \frac{\varepsilon - \Delta t\sigma}{\varepsilon} U_z^{n}(i,j,k) \\ A_z^{n+1}(i,j,k) &= A_z^{n}(i,j,k) + \frac{\Delta t}{\mu} U_z^{n}(i,j,k) \end{aligned} \tag{5}$$

Here, s_i are the stretched-coordinate metrics, which are defined as

$$s_i = \kappa_i + \frac{\sigma_i}{\alpha_i + j\omega\mu_0}, \quad (i = x, y, z) \tag{6}$$

where κ_i is the effective extension factor, α_i is the degree of freedom of the coordinate contraction–expansion factor whose field value is in the i direction, and σ_i is the electrical conductivity in the CPML boundary region.

The first formula of (5) can be expressed as

$$\begin{aligned} U_x^{n+1}(i,j,k) &= \frac{\varepsilon - \Delta t\sigma}{\varepsilon} U_x^{n}(i,j,k) \\ &\quad + \frac{\Delta t}{\varepsilon}\bar{s}_x \cdot \left(\frac{\partial^2 A_x^{n+1}}{\partial y^2} + \frac{\partial^2 A_x^{n+1}}{\partial z^2}\right) \end{aligned} \tag{7}$$

where $\bar{s}_x$ is the inverse Laplace transforms of $1/s_x$, and the convolution on the right side of the equation is computed using recursion convolution.

According to Laplace transform theory, the impulse response of $\bar{s}_i$ is as follows

$$\bar{s}_i(t) = \frac{\delta(t)}{\kappa_i} - \frac{\sigma_i}{\varepsilon_0 \kappa_i^2} e^{-\left(\frac{\sigma_i}{\varepsilon_0\kappa_i} + \frac{\alpha_i}{\varepsilon_0}\right)t} u(t) = \frac{\delta(t)}{\kappa_i} + \zeta_i(t) \tag{8}$$

where $u(t)$ and $\delta(t)$ are respectively the unit step function and unit impulse function.

By substituting (8) in (7), we obtain

$$\begin{aligned} U_x^{n+1}(i,j,k) &= \frac{\Delta t}{\varepsilon}\frac{1}{\kappa_x} \cdot \left(\frac{\partial^2 A_x^{n+1}}{\partial y^2} + \frac{\partial^2 A_x^{n+1}}{\partial z^2}\right) \\ &\quad + \frac{\varepsilon - \Delta t\sigma}{\varepsilon} U_x^{n}(i,j,k) + + \frac{\Delta t}{\varepsilon}\zeta_x(t) \\ &\quad \cdot \left(\frac{\partial^2 A_x^{n+1}}{\partial y^2} + \frac{\partial^2 A_x^{n+1}}{\partial z^2}\right) \end{aligned} \tag{9}$$

To improve the efficiency of convolution computation, the discrete impulse response is defined as

$$\begin{aligned} Z_i(m) &= \int_{m\Delta t}^{(m+1)\Delta t} \zeta_x(t) d\tau \\ &= -\frac{\sigma_i}{\varepsilon_0 \kappa_i^2} \int_{m\Delta t}^{(m+1)\Delta t} e^{-\left(\frac{\sigma_i}{\varepsilon_0\kappa_i} + \frac{\alpha_i}{\varepsilon_0}\right)\tau} d\tau \\ &= a_i e^{-\left(\frac{\sigma_i}{\kappa_i} + \alpha_i\right)\frac{m\Delta t}{\varepsilon_0}\tau} \end{aligned} \tag{10}$$

where

$$a_i = \frac{\sigma_i}{\left(\sigma_i\kappa_i + \kappa_i^2\alpha_i\right)}\left(e^{-\left(\frac{\sigma_i}{\kappa_i} + \alpha_i\right)\frac{\Delta t}{\varepsilon_0}} - 1.0\right) \tag{11}$$

The iterative equation of the first-order symplectic Euler algorithm can be obtained after simplifying (9)

$$\begin{aligned} U_x^{n+1}(i,j,k) &= \frac{\Delta t}{\varepsilon}\sum_{m=0}^{N-1} Z_x(m) \cdot \left(\frac{\partial^2 A_x^{n+1}}{\partial y^2} + \frac{\partial^2 A_x^{n+1}}{\partial z^2}\right) \\ &\quad + \frac{\varepsilon - \Delta t\sigma}{\varepsilon} U_x^{n}(i,j,k) + \frac{\Delta t}{\varepsilon}\frac{1}{\kappa_x} \\ &\quad \cdot \left(\frac{\partial^2 A_x^{n+1}}{\partial y^2} + \frac{\partial^2 A_x^{n+1}}{\partial z^2}\right) \end{aligned} \tag{12}$$

This equation involves a relatively complicated discrete convolution computation. Because has a simple exponential form, their sum can be obtained by recursive convolution. By introducing a new set of auxiliary expressions, (12) is rewritten as

$$\begin{aligned} U_x^{n+1}(i,j,k) &= \frac{\Delta t}{\varepsilon}\frac{1}{\kappa_x} \cdot \left(\frac{\partial^2 A_x^{n+1}}{\partial y^2} + \frac{\partial^2 A_x^{n+1}}{\partial z^2}\right) \\ &\quad + \frac{\Delta t}{\varepsilon}\left(\psi_{x1}^{n+1}(i,j,k) + \psi_{x2}^{n+1}(i,j,k)\right) \\ &\quad + \frac{\varepsilon - \Delta t\sigma}{\varepsilon} U_x^{n}(i,j,k) \end{aligned} \tag{13}$$

Here $\psi_{x1}^{n+1}(i,j,k)$ and $\psi_{x2}^{n+1}(i,j,k)$ can be calculated based on the following equations

$$\begin{aligned} &\psi_{x1}^{n+1}(i,j,k) \\ &= b_x \psi_{x1}^{n}(i,j,k) \\ &\quad + a_x \frac{A_x^{n+1}(i,j+\Delta y,k) - 2A_x^{n+1}(i,j,k) + A_x^{n+1}(i,j-\Delta y,k)}{\Delta y^2} \end{aligned} \tag{14}$$

$$\begin{aligned} &\psi_{x2}^{n+1}(i,j,k) \\ &= b_x \psi_{x2}^{n}(i,j,k) \\ &\quad + a_x \frac{A_x^{n+1}(i,j,k+\Delta z) - 2A_x^{n+1}(i,j,k) + A_x^{n+1}(i,j,k-\Delta z)}{\Delta z^2} \end{aligned} \tag{15}$$

where b_i is defined as

$$b_i = e^{-\left(\frac{\sigma_i}{\kappa_i}+\alpha_i\right)\frac{\Delta t}{\varepsilon_0}}, \quad (i = x, y) \tag{16}$$

It can be seen from the above formula that the public form of the front part is similar to that of the conventional symplectic algorithm except for item κ and the following ψ. The remaining field quantities can be derived in the same way. The parameters κ, α, and σ in the PML layer of CPML change monotonously. In the case of the x direction, the following equation is often adopted

$$\begin{aligned} \sigma(x) &= \frac{\sigma_{\max}|x - x_0|^m}{d^m} \\ \kappa(x) &= 1 + (\kappa_{\max} - 1)\frac{|x - x_0|^m}{d^m} \\ \alpha(x) &= \frac{\alpha_{\max}|x - x_0|}{d} \end{aligned} \tag{17}$$

Here, d is the thickness of the PML layer, and x0 is the number of grids at the boundary between the PML layer and the simulated region. In the simulation, $d = 10$, $m = 4$, $\alpha_{\max} = 0.008$, $\kappa_{\max} = 5$, and $\sigma_{\max} = \frac{m+1}{\sqrt{\varepsilon_r}150\pi\delta}$, where δ simulates the size of the grid.

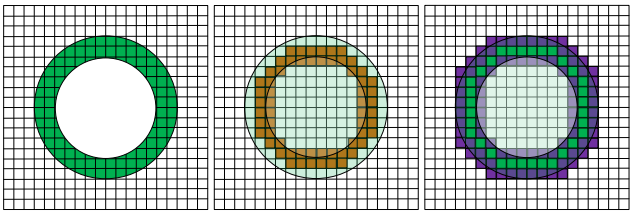

FIGURE 2. Subdivided grids of circular pipeline. (a) Actual subdivided grids of circular pipeline. (b) Subdivided grids of circular pipeline's actual simulation computation obtained through ladder approximation. (c) Subdivided grids of circular pipeline obtained based on conformal grid method.

III. CUDA-IMPLEMENTED CONFORMAL SYMPLECTIC EULER ALGORITHM

A. SURFACE CONFORMAL TECHNOLOGY

In this study, a conformal grid method based on effective medium parameters is adopted to simulate the circular boundaries of underground pipelines [30], [31]. The actual subdivided grids of the circular pipeline are shown in Fig. 2(a), where the white grids are the normal grid points and the green grids are the actual subdivided grids of the pipeline. Fig. 2(b) shows the subdivided grids of the circular pipeline's actual simulation computation obtained through ladder approximation, while the orange grids of the pipeline are gained through conventional ladder approximation. The subdivided grids of the circular pipeline based on the conformal grid method are shown in Fig. 2(c), where the purple grids are conformal, and the other grids are non-conformal.

The conformal grid units are extracted from Fig. 2(c), which indicates the equivalent medium parameter relationship of the conformal grid points of the non-ideal conductor

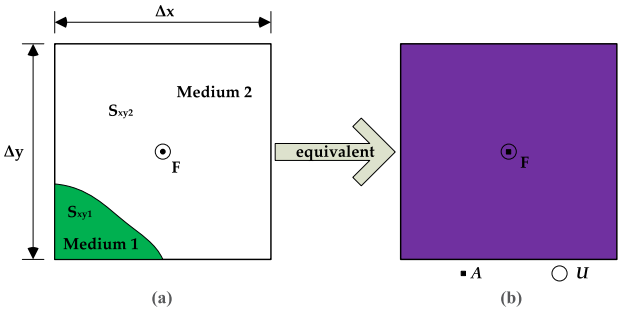

FIGURE 3. Equivalent medium parameters of conformal grid points. (a) Actual subdivided grids. (b) Conformal grids.

medium in the two-dimensional TM wave. In the symplectic Euler algorithm, the $\boldsymbol{U}$ and $\boldsymbol{A}$ are defined at the same space grid node and the same time step. The computation of the conformal grid points is shown in Fig. 3, where **F** is the sampling point of the $\boldsymbol{U}$ and $\boldsymbol{A}$, Δy and Δx are the height and width of the grid, and S_{xy1} and S_{xy2} are the areas of mediums 1 and 2, respectively. The electromagnetic parameters of mediums 1 and 2 are assumed to be σ_1, ε_1, μ_1 and σ_2, ε_2, μ_2. The $\boldsymbol{A}$ and $\boldsymbol{U}$ are located at the center of the grid units. The effective values of the dielectric constant, electrical conductivity, and magnetic conductivity are obtained based on the weighted average of the area of the grids occupied by different mediums.

As shown in Fig. 3(b), the electrical conductivity, equivalent dielectric constant and magnetic conductivity at the sampling point F of field components are

$$\begin{aligned} \varepsilon_z^{eff}(F) &= \left[S_{xy1}\varepsilon_1 + S_{xy2}\varepsilon_2\right]/\Delta x\Delta y \\ \sigma_z^{eff}(F) &= \left[S_{xy1}\sigma_1 + S_{xy2}\sigma_2\right]/\Delta x\Delta y \\ \mu_z^{eff}(F) &= \left[S_{xy1}\mu_1 + S_{xy2}\mu_2\right]/\Delta x\Delta y \end{aligned} \tag{18}$$

where *eff* represents the equivalent of a parameter.

By substituting (18) in (4), the iterative differential equation of the conformal symplectic Euler algorithm is obtained as

$$\begin{aligned} A_{i,j}^{n+1} &= A_{i,j}^{n} + \frac{dt}{\mu^{eff}}U_{i,j}^{n} \\ U_{i,j}^{n+1} &= \frac{\varepsilon^{eff} - dt\sigma^{eff}}{\varepsilon^{eff}}U_{i,j}^{n} + \frac{dt}{\varepsilon^{eff}}\nabla^2 A_{i,j}^{n+1} \end{aligned} \tag{19}$$

The conformal grid points of the ideal conductor in the two-dimensional TM wave are different from those of the non-ideal conductor. The computation of the conformal grid points of the ideal conductor is shown in Fig. 4.

where **F** is the sampling point of the $\boldsymbol{U}$ and $\boldsymbol{A}$, Δy and Δx are the height and width of the grid, and S_{xy1} and S_{xy2} are the areas of mediums 1 and 2, respectively. The mediums 1 is an additional layer of PEC material created essentially in metallic objects.The $\boldsymbol{A}$ and $\boldsymbol{U}$ are located at the center of the grid units. The effective values of the dielectric constant, electrical conductivity, and magnetic conductivity are obtained based on the weighted average of the area of the grids occupied by different mediums except the ideal conductor.

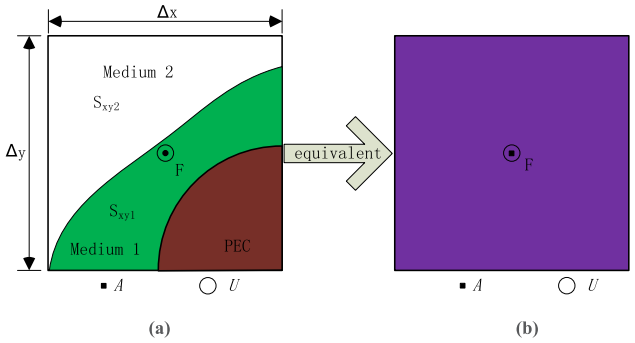

FIGURE 4. Equivalent medium parameters of conformal grid points of the ideal conductor. (a) Actual subdivided grids. (b) Conformal grids.

As shown in Fig. 4(b), the electrical conductivity, equivalent dielectric constant and magnetic conductivity at the sampling point F of field components are

$$\begin{aligned} \varepsilon_z^{eff}(F) &= \left[S_{xy1}\varepsilon_1 + S_{xy2}\varepsilon_2\right] / \left(S_{xy1} + S_{xy2}\right) \\ \sigma^{eff}(F) &= \left[S_{xy1}\sigma_1 + S_{xy2}\sigma_2\right] / \left(S_{xy1} + S_{xy2}\right) \\ \mu^{eff}(F) &= \left[S_{xy1}\mu_1 + S_{xy2}\mu_2\right] / \left(S_{xy1} + S_{xy2}\right) \end{aligned} \quad (20)$$

where *eff* represents the equivalent of a parameter.

B. GPU PARALLEL COMPUTING OF CONFORMAL SYMPLECTIC EULER ALGORITHM

Compute unified device architecture (CUDA) can efficiently execute many complex computing tasks through the parallel computing realized by the NVIDIA GPU [32]–[35], which is suitable for solving parallel computing problems. The parallel conformal symplectic Euler algorithm implemented on a GPU differs from the traditional serial symplectic Euler algorithm implemented on a CPU in that the former is executed on different devices with a similar execution process. The two-dimensional symplectic algorithm problem is initially divided into rough sub-problems, e.g., system initialization and modeling, magnetic and electric field updates, and data output. The field value is set to zero in system initialization and modeling. The system parameters are assigned by reading the input files, e.g., the forward numerical model and excitation source. As a serial part of the program, data output is executed on the CPU. On the GPU, the updates of field components $\boldsymbol{A}$ and $\boldsymbol{U}$ are independent, and $\boldsymbol{A}$ is updated before $\boldsymbol{U}$. These two computationally intensive sub-problems (kernel functions) are executed on the GPU. Fig. 5 shows the flowchart of the two-dimensional parallel conformal symplectic algorithm on the GPU.

Field components $\boldsymbol{A}_z$ and $\boldsymbol{U}_z$ are computed in the two-dimensional x-y square domain in the parallel symplectic algorithm. The number of threads is determined by the computational domain, i.e., the number of symplectic partitioned units. Two CUDA kernel functions are required to deal with the two-dimensional conformal symplectic algorithm problem. The first kernel function is to compute $\boldsymbol{A}_z$, and the second is to update $\boldsymbol{U}_z$. As shown in Fig. 6, each thread is

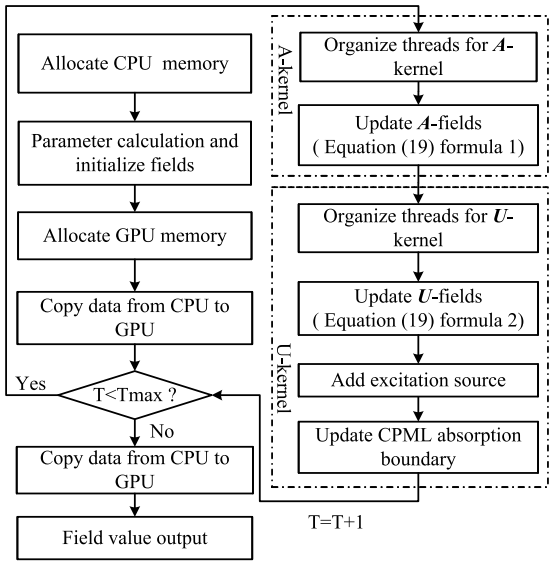

FIGURE 5. Flowchart of parallel conformal symplectic algorithm.

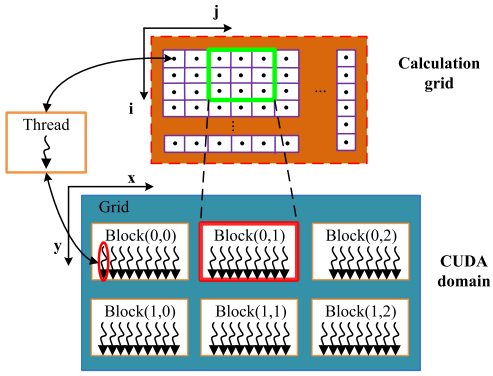

FIGURE 6. Threads of two-dimensional parallel conformal symplectic algorithm.

responsible for computing a symplectic partitioned unit, each thread block is supposed to compute a set of consecutive symplectic partitioned units, and parallel computation is performed on the entire computational domain according to the above strategy.

The two-dimensional line source propagation model is used to verify the accuracy of the proposed algorithm and the absorption effect of the CPML boundary conditions. Visual Studio 2010 and CUDA Toolkit 7.5 are used as the development tools, and the Intel Core i7-6700K equipped with the NVIDIA GeForce GTX 1070 serves as the central processor. The simulation area is a 200 cm × 200 cm rectangle, with air as the internal medium, and a Ricker wavelet with a center frequency of 1 GHz is added to the center of the simulation area (Fig. 7). The time step and spatial step are 0.01 ns and 0.5 cm, respectively. Fig. 8 shows snapshots of the wave field at different time points. It can be seen from the figure that the CPML absorption boundary conditions are quite favorable.

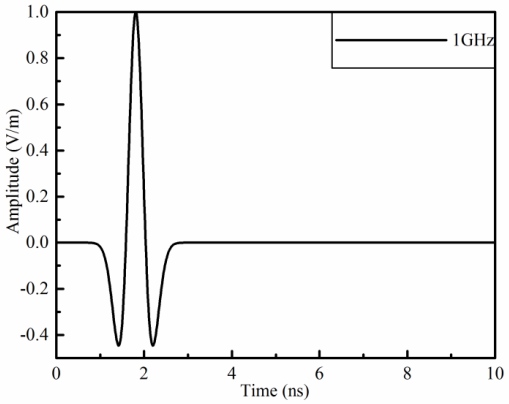

FIGURE 7. Waveform of Ricker wavelet with center frequency of 1 GHz.

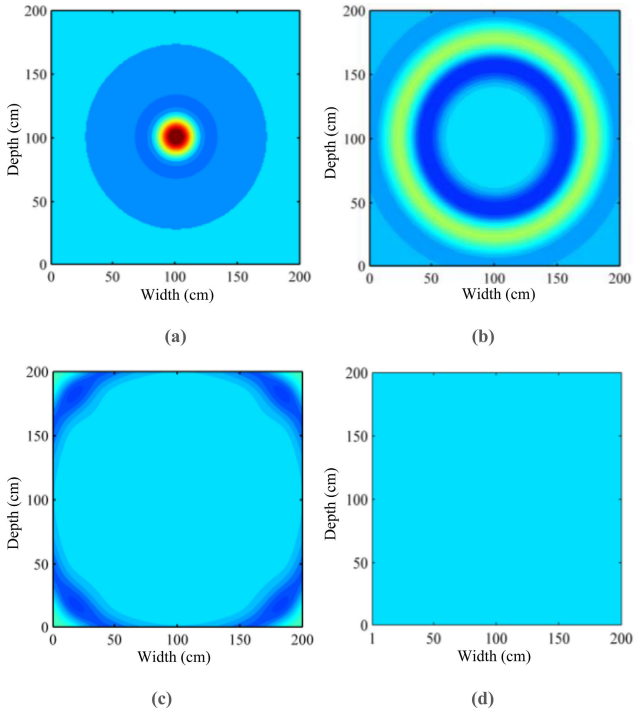

FIGURE 8. Distribution of component Ez at different times: (a) The distribution of component Ez at 2ns. (b) The distribution of component Ez at 3ns. (c) The distribution of component Ez at 4ns. (d) The distribution of component Ez at 5ns.

IV. NUMERICAL SIMULATIONS

A. TWO-LAYER MEDIUM MODEL WITH CIRCULAR VOIDS

The accuracy and efficiency of the algorithm were verified by the two-layer medium model with circular voids shown in Fig. 9. On the ground, the GPR launched in the air moved along the B-scanning line and continuously transmitted to the ground or received waves from the ground so as to gain the B-scanning data. The B-scanning line horizontally moved by 2 m in this model. The underground part of the model consists of two layers, the upper being an air layer 0.2 m thick, and the lower one a clay layer 0.8 m thick. In the clay layer, there is a circular void with a diameter of 0.1 m at a depth

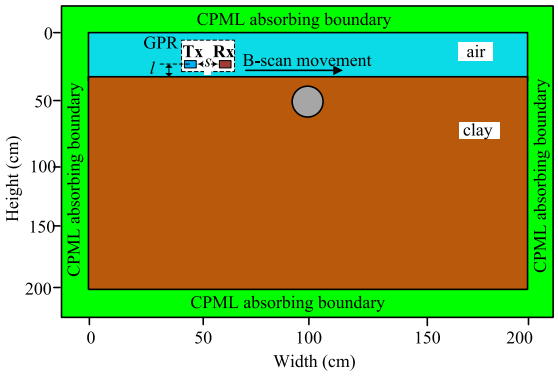

FIGURE 9. Schematic diagram of two-layer medium model containing circular voids.

TABLE 1. Dielectric constant and conductivity of different media.

Material	ε_r	σ(S/m)
Air	1	0
Water	81	0
PVC plastic	3	0
Concrete	6	0.001
Clay	12	0.002
Metal	1	1.0×10^6

of 0.25 m, which has a conductivity $\sigma = 0$ mS/m, and a relative dielectric constant $\varepsilon_r = 30$. In this model, the time step and spatial increment were set as $\Delta t = 0.01$ ns and $\Delta x = \Delta y = 0.005$ m, and the relative magnetic conductivity μ of all materials was assumed to be 1. The Ricker wavelet with a center frequency of 1 GHz was selected as the excitation source, the interval s between the transmitter Tx and the receiver Rx was 0.1 m, and the distance l from the transmitter Tx to the clay layer was 0.05 m. The CPML absorption boundary conditions were adopted outside the computational domain, and the thickness of CPML was set as $d = 0.08$ m. Table 1 shows the relative dielectric constant ε and electrical conductivity σ of different mediums in the model.

To verify the efficiency and accuracy of the proposed algorithm, we simulated this model using the parallel conformal symplectic Euler algorithm and the serial non-conformal symplectic Euler algorithm, and solved this model numerically. Fig. 10 shows the GPR B-scan images obtained by the simulation conducted by the serial non-conformal symplectic Euler algorithm and the parallel conformal symplectic Euler algorithm. The parallel conformal symplectic Euler algorithm requires 110.998 s, and the serial non-conformal symplectic Euler algorithm requires 1118.796 s. The parallel conformal symplectic Euler algorithm realized on the GPU saves 90.08% of the computation time of the serial non-conformal symplectic Euler algorithm. According to Fig. 10, in the circular cavity simulation, the parallel conformal symplectic Euler algorithm can significantly reduce the error caused by the conventional ladder approximation and improve the computational efficiency, thereby increasing the simulation accuracy.

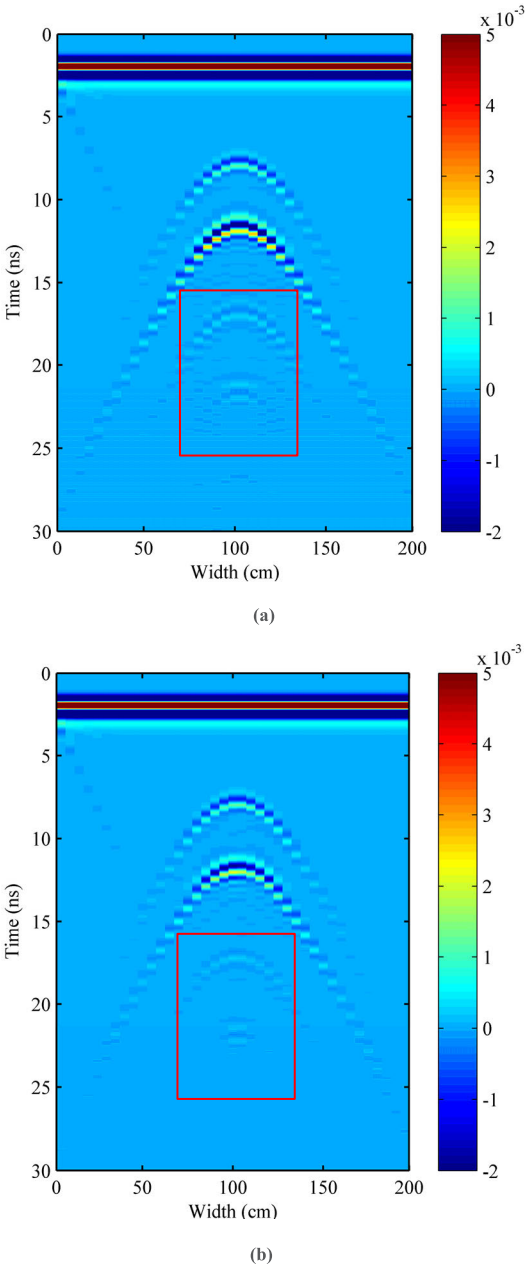

FIGURE 10. Simulation results of GPR B-scan images. (a) Simulation results obtained by serial non-conformal symplectic Euler algorithm. (b) Simulation results obtained by parallel conformal symplectic Euler algorithm.

B. CONCRETE PIPELINE MODEL

The numerical model is a 1:1 underground concrete pipeline model. The pipeline is assumed to be uniform, infinitely long, and perpendicular to the two-dimensional plane defining the pipeline (Fig. 11). The pipeline is made of concrete, the pipeline wall is 0.1 m thick, the diameter is 1 m, and the top of the pipeline is 1.3 m below the ground surface. The time step and spatial increment are set as $\Delta t = 0.01$ ns, $\Delta x = \Delta y = 0.005$ m, and the simulation consists of 5,000 time steps. Table 1 shows the relative dielectric constant ε and electrical conductivity σ of different mediums in the model.

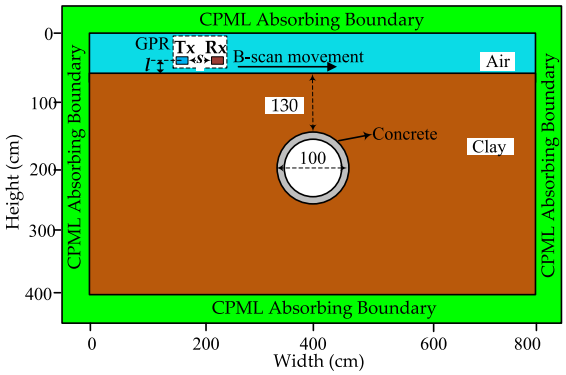

FIGURE 11. Schematic diagram of underground concrete pipeline model.

The relative magnetic conductivity μ of all materials is assumed to be 1. The same excitation source as in Model 1 is selected, and the GPR system is set the same as well. The electromagnetic responses of the GPR are simulated when air and water are inside the pipeline.

Fig. 12 shows the GPR B-scan images obtained by parallel conformal symplectic Euler algorithm of the underground concrete pipeline models filled with air and water. As shown in Fig. 12(a), A and B are the reflections at the top and bottom of the concrete pipeline, and C is the multiple reflection waveform inside the pipeline. According to the figure, the reflection at the top and bottom of the pipeline is more obvious, and the multiple reflections inside the pipeline are closer to the actual situation. It can be seen from Fig. 12(b) that A and B are the reflections of the top and bottom of the concrete pipeline. Because of water absorbs electromagnetic waves relatively strongly, the reflection at the bottom of the pipe is not obvious and there are no multiple reflection waveforms in the pipeline.

According to Fig. 12(a) and Fig. 12(b), the characteristics of the GPR B-scan images of the underground concrete pipeline model differ greatly in different situations, i.e., when the pipeline is empty, and filled with water. Particularly obvious diffraction hyperbola features are found in the GPR B-scan image of the model of the underground concrete pipeline filled with air, and the multiple reflections at the bottom of the pipeline and inside it are comparatively apparent. Regarding the model of the pipeline filled with water, the diffraction hyperbola features are only obvious at the top of the pipeline, while due to the absorptivity of water, multiple reflections at the bottom and inside the pipeline have hardly any hyperbola features. By analyzing the diffraction hyperbola features and time of the GPR data, the position of the pipeline and the condition inside it can be accurately determined.

C. METAL AND PVC PIPELINE MODEL

This model is a 1:1 actual underground metal and PVC plastic pipe model, as shown in Fig.13. In this model, the pipeline materials are metal and PVC, respectively. The pipeline wall

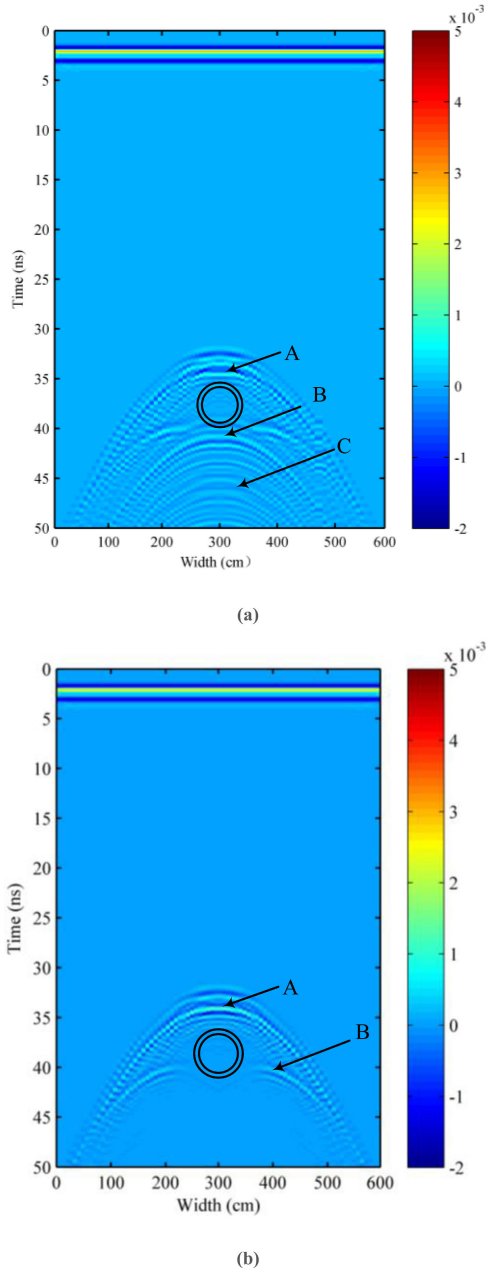

FIGURE 12. Simulation results of GPR B-scan images. (a) Simulation results of concrete pipeline model filled with air. (b) Simulation results of concrete pipeline model filled with water.

is 0.02 cm thick, the diameter is 0.3 cm, and the top of the pipeline is 0.7 cm below the ground surface. The spatial increment and time step are set as $\Delta x = \Delta y = 0.0025$ m and $\Delta t = 0.005$ ns, respectively, and the simulation has 5,000 time steps. Table 1 shows the relative dielectric constant ε and electrical conductivity σ of different mediums in the model. The relative magnetic conductivity μ of all materials is assumed to be 1. The same excitation source as in Model 1 is selected, and the GPR system is set as in Model 1. The electromagnetic responses of the GPR are simulated when there are air and water inside the PVC pipeline and there is air inside metal pipeline.

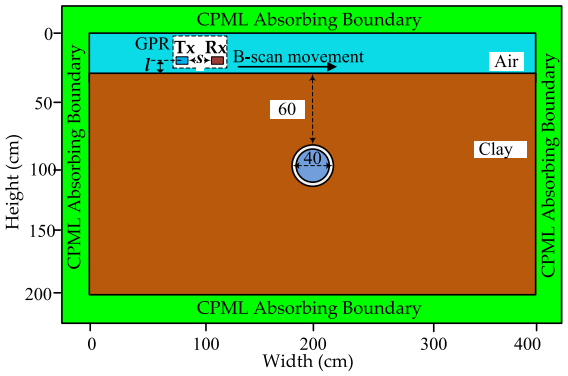

FIGURE 13. Schematic diagram of underground PVC and metal pipeline model.

Fig.14 shows the GPR B-scan images of the model of the underground PVC pipeline filled with air and water and metal pipe filled with air obtained by parallel conformal symplectic Euler algorithm. As shown in Fig. 14(a), A and B are the reflections at the top and bottom of the PVC pipeline, and C is the reflection waveform inside the pipeline. According to the figure, the reflection from the bottom and top of the pipe is superimposed, and the reflection from the inside of the pipe is almost none, because the pipe radius is small and the dielectric property of PVC material is close to clay. It can be seen from Fig. 14(b) that A and B are the reflections at the top and bottom of the PVC pipe, and C is the multiple reflection waveform inside the pipe. Due to the small diameter of the pipe and the dielectric properties of PVC close to that of clay, the water-filled PVC pipe shows only the basic characteristics of water in the GPR B scan. As shown in Fig. 14(c), A is the reflection at the top of the metal pipeline, C is the reflection waveform inside the pipe. It can be seen from Fig. 14(c) that obvious diffraction hyperbola features can be found in the GPR B-scan image of the model of the underground metal pipeline filled with air. Due to the absorptivity of metal, multiple reflections at the bottom of the pipeline and inside the pipeline have hardly any hyperbola features.

According to Fig. 14(a) and Fig. 14(b), the characteristics of the GPR B-scan images of the model of the underground PVC pipeline filled with air and water differ greatly. Because of the smaller diameter of the pipe and the similar dielectric properties of PVC with clay, the GPR B-scan image of the underground PVC pipe filled with air model only has particularly obvious diffraction hyperbola features on the top of the pipe. For the model of the PVC pipeline filled with water, the diffraction hyperbola feature is obvious in pipe top and bottom, and the hyperbola feature of multiple reflections is also present inside of the pipe. Because of the high reflectivity and attenuation of the metal, the GPR B scan image of Fig. 14(c) only has obvious hyperbolic characteristics on the top of the pipe. By analyzing the diffraction hyperbola features and time of the GPR data, the material of pipeline and the condition inside the pipeline can be accurately determined.

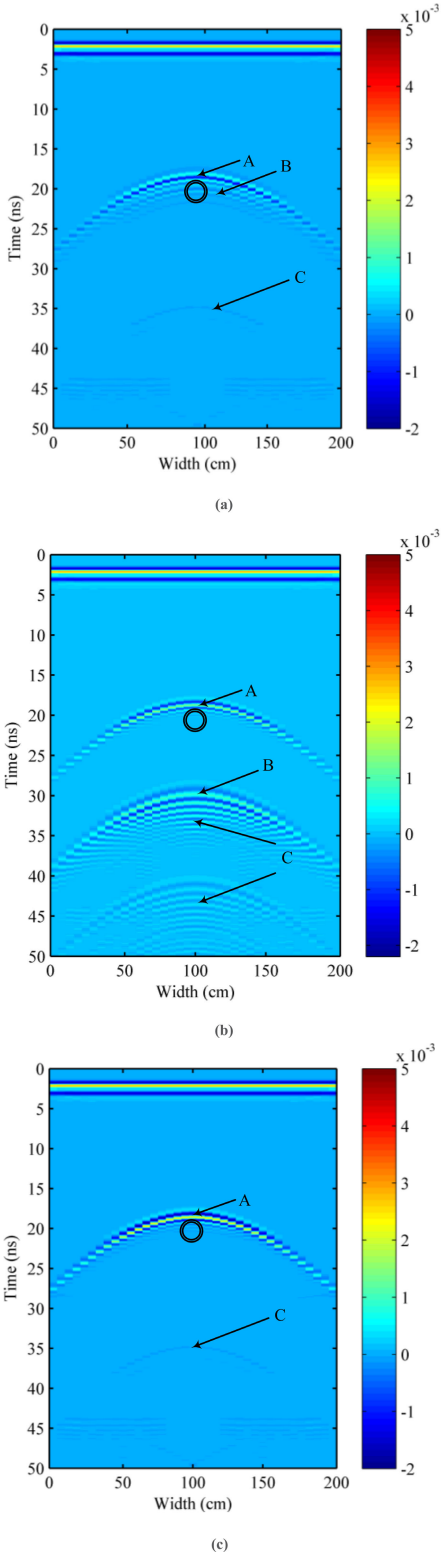

FIGURE 14. Simulation results of GPR B-scan images. (a) Simulation results of underground PVC pipeline filled with air. (b) Simulation results of underground PVC pipeline filled with water. (c) Simulation results of underground metal pipeline filled with air.

V. CONCLUSION

In this study, an accurate and efficient numerical model of GPR in different underground pipeline structures was established based on the symplectic Euler algorithm, surface conformal technology and GPU acceleration method, realizing accurate and efficient computation of electromagnetic responses of different underground pipelines. The simulation results show that surface conformal technology can greatly reduce the error caused by the conventional ladder approximation of circular boundaries and GPU acceleration method can save greater than 90% of the computation time compared with the serial non-conformal symplectic Euler algorithm in forward numerical computation. This accurate and efficient GPR forward model can better interpret the measured GPR data and present the distinctive features of the measured GPR data of a metal pipeline, plastic pipeline filled with air and water, and concrete pipeline. By analyzing the diffraction hyperbola features and time of the GPR data, the material of pipeline and position of the pipeline and the condition inside it can be accurately determined. In the next step, we will extend the algorithm to three-dimensional simulation research and improve the processing efficiency and interpretation accuracy of 3D GPR detection data in non-destructive testing (NDT) of underground pipes, and provide an efficient forward model for the GPR 3D inversion imaging.

REFERENCES

[1] P. Zhang, X. Guo, N. Muhammat, and X. Wang, "Research on probing and predicting the diameter of an underground pipeline by GPR during an operation period," *Tunnelling Underground Space Technol.*, vol. 58, pp. 99–108, Sep. 2016.
[2] J. F. C. Sham, W. W. L. Lai, W. Chan, and C. L. Koh, "Imaging and condition diagnosis of underground sewer liners via active and passive infrared thermography: A case study in singapore," *Tunnelling Underground Space Technol.*, vol. 84, pp. 440–450, Feb. 2019.
[3] E. Pettinelli, A. Di Matteo, E. Mattei, L. Crocco, F. Soldovieri, J. D. Redman, and A. P. Annan, "GPR response from buried pipes: Measurement on field site and tomographic reconstructions," *IEEE Trans. Geosci. Remote Sens.*, vol. 47, no. 8, pp. 2639–2654, Aug. 2009.
[4] A. Cataldo, R. Persico, G. Leucci, E. De Benedetto, G. Cannazza, L. Matera, and L. De Giorgi, "Time domain reflectometry, ground penetrating radar and electrical resistivity tomography: A comparative analysis of alternative approaches for leak detection in underground pipes," *NDT E Int.*, vol. 62, pp. 14–28, Mar. 2014.
[5] F. Soldovieri, A. Brancaccio, G. Prisco, G. Leone, and R. Pierri, "A kirchhoff-based shape reconstruction algorithm for the multimonostatic configuration: The realistic case of buried pipes," *IEEE Trans. Geosci. Remote Sens.*, vol. 46, no. 10, pp. 3031–3038, Oct. 2008.
[6] L. A. Varyanitza-Roshchupkina and G. P. Pochanin, "Strategy of GPR searching for low radar contrast plastic pipes in ground," *IEEE Aerosp. Electron. Syst. Mag.*, vol. 21, no. 12, pp. 23–26, Dec. 2006.
[7] Q. Di, M. Zhang, and M. Wang, "Time-domain inversion of GPR data containing attenuation due to conductive losses," *Geophysics*, vol. 71, no. 5, pp. K103–K109, Sep. 2006.
[8] F. De-shan and D. Qian-wei, "GPR numerical simulation of full wave field based on UPML boundary condition of ADI-FDTD," *NDT E Int.*, vol. 44, no. 6, pp. 495–504, Oct. 2011.
[9] C. Yuan, S. Li, H. Cai, and V. R. Kamat, "GPR signature detection and decomposition for mapping buried utilities with complex spatial configuration," *J. Comput. Civil Eng.*, vol. 32, no. 4, Jul. 2018, Art. no. 04018026.
[10] I. Giannakis, A. Giannopoulos, and C. Warren, "Realistic FDTD GPR antenna models optimized using a novel linear/nonlinear full-waveform inversion," *IEEE Trans. Geosci. Remote Sens.*, vol. 57, no. 3, pp. 1768–1778, Mar. 2019.
[11] Z. Xiong and A. C. Tripp, "3-D electromagnetic modeling for near-surface targets using integral equations," *Geophysics*, vol. 62, no. 4, pp. 1097–1106, Jul. 1997.
[12] X. Zeng and G. A. Mcmechan, "GPR characterization of buried tanks and pipes," *Geophysics*, vol. 62, no. 3, pp. 797–806, May 1997.

[13] R. L. Roberts and J. J. Daniels, "Modeling near-field GPR in three dimensions using the FDTD method," *Geophysics*, vol. 62, no. 4, pp. 1114–1126, Jul. 1997.

[14] L. Crocco, G. Prisco, F. Soldovieri, and N. J. Cassidy, "Advanced forward modeling and tomographic inversion for leaking water pipes monitoring," in *Proc. 4th Int. Workshop, Adv. Ground Penetrating Radar*, Jun. 2007, pp. 113–117.

[15] Y. Huang, J. Zhang, and Q. H. Liu, "Three-dimensional GPR ray tracing based on wavefront expansion with irregular cells," *IEEE Trans. Geosci. Remote Sens.*, vol. 49, no. 2, pp. 679–687, Feb. 2011.

[16] X. Zhou, H. Chen, and J. Li, "An automatic GPR B-Scan image interpreting model," *IEEE Trans. Geosci. Remote Sens.*, vol. 56, no. 6, pp. 3398–3412, Jun. 2018.

[17] J. M. Bourgeois and G. S. Smith, "A fully three-dimensional simulation of a ground-penetrating radar: FDTD theory compared with experiment," *IEEE Trans. Geosci. Remote Sens.*, vol. 34, no. 1, pp. 36–44, Jan. 1996.

[18] H. Fang, G. Lin, and R. Zhang, "The first-order symplectic euler method for simulation of GPR wave propagation in pavement structure," *IEEE Trans. Geosci. Remote Sens.*, vol. 51, no. 1, pp. 93–98, Jan. 2013.

[19] S. Zhao and I. Al-Qadi, "Pavement drainage pipe condition assessment by GPR image reconstruction using FDTD modeling," *Construction Building Mater.*, vol. 154, pp. 1283–1293, Nov. 2017.

[20] J. Lachowicz and M. Rucka, "3-D finite-difference time-domain modelling of ground penetrating radar for identification of rebars in complex reinforced concrete structures," *Arch Civ. Mech Eng.*, vol. 18, no. 4, pp. 1128–1140, Sep. 2018.

[21] D. Feng, X. Wang, and B. Zhang, "Specific evaluation of tunnel lining multi-defects by all-refined GPR simulation method using hybrid algorithm of FETD and FDTD," *Construct. Building Mater.*, vol. 185, pp. 220–229, Oct. 2018.

[22] H. Fang, J. Lei, M. Yang, and Z. Li, "Analysis of GPR wave propagation using CUDA-implemented conformal symplectic partitioned Runge-Kutta method," *Complexity*, vol. 2019, pp. 1–14, Jun. 2019.

[23] H. Fang, J. Lei, J. Zhang, J. An, and F. Wang, "Modelling GPR wave propagation using GPU parallel implementation of the symplectic euler method," *Near Surf. Geophys.*, pp. 417–425, Jul. 2019.

[24] J. Lei, Z. Wang, H. Fang, X. Ding, X. Zhang, M. Yang, and H. Wang, "Analysis of GPR wave propagation in complex underground structures using CUDA-implemented conformal FDTD method," *Int. J. Antennas Propag.*, vol. 2019, pp. 1–11, Aug. 2019.

[25] L.-L. Jiang, J.-F. Mao, and X.-L. Wu, "Symplectic finite-difference time-domain method for maxwell equations," *IEEE Trans. Magn.*, vol. 42, no. 8, pp. 1991–1995, Aug. 2006.

[26] T. Monovasilis, Z. Kalogiratou, and T. E. Simos, "Symplectic partitioned Runge-Kutta methods with minimal phase-lag," *Comput. Commun.*, vol. 181, no. 7, pp. 1251–1254, Jul. 2010.

[27] H. Fang and G. Lin, "Symplectic partitioned Runge-Kutta methods for two-dimensional numerical model of ground penetrating radar," *Comput. Geosci.*, vol. 49, pp. 323–329, Dec. 2012.

[28] J. A. Roden and S. D. Gedney, "Convolution PML (CPML): An efficient FDTD implementation of the CFS-PML for arbitrary media," *Microw. Opt. Technol. Lett.*, vol. 27, no. 5, pp. 334–339, Dec. 2000.

[29] A. Giannopoulos, "Multipole perfectly matched layer for finite-difference time-domain electromagnetic modeling," *IEEE Trans. Antennas Propag.*, vol. 66, no. 6, pp. 2987–2995, Jun. 2018.

[30] T. Su, Y. Liu, W. Yu, and R. Mittra, "A conformal mesh-generating technique for the conformal finite-difference time-domain (CFDTD) method," *IEEE Antennas Propag. Mag.*, vol. 46, no. 1, pp. 37–49, Feb. 2004.

[31] G. Junkin, "Conformal FDTD modeling of imperfect conductors at millimeter wave bands," *IEEE Trans. Antennas Propag.*, vol. 59, no. 1, pp. 199–205, Jan. 2011.

[32] J. Chi, F. Liu, E. Weber, Y. Li, and S. Crozier, "GPU-accelerated FDTD modeling of radio-frequency Field–Tissue interactions in high-field MRI," *IEEE Trans. Biomed. Eng.*, vol. 58, no. 6, pp. 1789–1796, Jun. 2011.

[33] C. Spa, A. Rey, and E. Hernandez, "A GPU implementation of an explicit compact FDTD algorithm with a digital impedance filter for room acoustics applications," *IEEE/ACM Trans. Audio, Speech, Language Process.*, vol. 23, no. 8, pp. 1368–1380, Aug. 2015.

[34] *NVIDIA CUDA C Programming Guide, Version 9.1*, NVIDIA, Santa Clara, CA, USA, 2017.

[35] C. Warren, A. Giannopoulos, A. Gray, I. Giannakis, A. Patterson, L. Wetter, and A. Hamrah, "A CUDA-based GPU engine for gprMax: Open source FDTD electromagnetic simulation software," *Comput. Phys. Commun.*, vol. 237, pp. 208–218, Apr. 2019.

JIANWEI LEI was born in Inner Mongolia, China, in 1993. He received the B.S. degree in road bridge and river-crossing engineering from Zhengzhou University, Zhengzhou, China, in 2016, where he is currently pursuing the Ph.D. degree in safety and protection engineering.

His research interests include nondestructive detection technique in engineering and numerical simulation methods (e.g., finite-difference time-domain method and symplectic methods).

BINGHAN XUE was born in Henan, China, in 1991. He received the Ph.D. degree in hydraulic structure engineering from the Dalian University of Technology, in 2018.

He is currently a Lecturer with the School of Water Conservancy Engineering, Zhengzhou University, Zhengzhou, China. His research interests include scaled boundary isogeometric analysis, mortar methods, and their applications in contact problems and electromagnetic field.

HONGYUAN FANG was born in Henan, China, in 1982. He received the B.S. and M.S. degrees in high-way and railway engineering from Zhengzhou University, Zhengzhou, China, in 2005 and 2008, respectively.

He is currently a Professor with the School of Water Conservancy Engineering, Zhengzhou University. He is now mainly engaged in non-destructive testing and trenchless repair theory and technology research of underground pipelines and other infrastructure projects.

YINPING LI was born in Chongqing, China, in 1997. She received the B.E. degree from Zhengzhou University, Henan, China, in 2019. She is currently pursuing the M.S. degree in geotechnical engineering with the School of Water Conservancy Engineering, Zhengzhou University, Zhengzhou, China.

Her research interests include three-dimensional tomography and migration imaging of ground penetrating radar(GPR).

MAN YANG was born in Henan, China, in 1987. She received the B.S. and M.S. degrees in water conservancy and hydropower engineering from Zhengzhou University, Zhengzhou, China, in 2010 and 2013, respectively, where she is currently pursuing the Ph.D. degree in high-way and railway engineering.

Her research interests include nondestructive detection technique in engineering and numerical simulation methods (e.g., finite-difference time-domain method, finite-element method, and symplectic methods).